A High Efficiency Force Predicting Method of Multi-axis Machining Propeller Blades

Zerun Zhu[1], Rong Yan[1], Fangyu Peng[2(✉)], Kang Song[1], Zepeng Li[1], Chaoyong Guo[1], and Chen Chen[1]

[1] National NC System Engineering Research Center, School of Mechanical Science and Engineering, Huazhong University of Science and Technology, Wuhan 430074, China

[2] State Key Laboratory of Digital Manufacturing Equipment and Technology, School of Mechanical Science and Engineering, Huazhong University of Science and Technology, 1037 Luoyu Road, Hongshan District, Wuhan 430074, Hubei, People's Republic of China
zwm8917@263.net

Abstract. Accurate cutting force prediction is a vital factor to analyze vibration, deformation, and residual stress in the machining. Meanwhile, it provides important reference for feed speed and tool orientation optimization. The problems of predicting accuracy and efficiency of cutting forces are serious especially for the 5-axis machining. Thus a rapid cutting force prediction method based on the classic mechanical model is proposed to calculate the 5-axis machining cutting forces. In the method, the cutting forces are directly calculated by elementary function integral, which can improve the calculating efficiency, compared with discretization and accumulation method. The experiments were conducted to verify the validity of the proposed method. The results show that the proposed method increases efficiency nearly 86 times compared with the z-map method and 20 times compared with the cutter/workpiece engagement boundary method and keeps a good accuracy.

Keywords: Multi-axis machining · Cutting forces · Highly efficiency prediction

1 Introduction

Accurate cutting force prediction is a vital factor to analyze vibration, deformation, and residual stress in the machining. Meanwhile, it provides important reference for feed rate and tool orientation optimization. The accuracy and efficiency of cutting forces prediction have great influences on the reliability and practicality of those works mentioned above. As a result, it is necessary to provide a rapid cutting force prediction method in the 5-axis machining.

In order to model instantaneous undeformed chip thickness(IUCT) which reflected the changes of the attitude angle in five-axis machining, as analyzing in reference [1] two methods are used: one is the vector projection method [2–4] from the total feed vector including linear and angular feed mode to the unit vector on the tool envelope

N. Kubota et al. (Eds.): ICIRA 2016, Part I, LNAI 9834, pp. 685–696, 2016.
DOI: 10.1007/978-3-319-43506-0_59

surface normal direction, the other is geometrical calculation method [5–8] of calculating the segment length on the IUCT defined line between the cutting edge element (CEE) and the cutter edge trajectory sweeping surface of the front cutting edge. In reference [1], the parametric model of IUCT is deduced and expressed as three sub models about tool orientation, tool orientation change and cutter runout, and this model is used in this paper for higher computational efficiency.

Determining the engaged cutting edge is also a main limitation in 5-axis milling. *Larue* and *Altintas* [9] used ACIS solid modeling environment to determine the engagement region for force simulations of flank milling, *Kim* et al. [10] and Zhu [5] determined the cutter contact area from the Z-map of the surface geometry and current cutter location. *Ozturk* and *Budak* [4] presented a complete geometry and force model for 5-axis milling operations using ball-end mills, and analyzed the effect of lead and tilt angles on the process geometry in detail. In the work of *Ozturk* [11] three boundary of CWE area were modeled and used to simulated cutting forces efficiently. Here, the boundary model was used and developed to improve the efficiency further more.

Compared with the previous work, the main contribution of this paper are: (1) the upper and lower boundary of the in-cutting cutter flute were calculated based on the boundary model, (2) the elementary integral model was developed and utilized to simulate propeller machining cutting forces. The remaining part of this paper is organized as follows. In Sect. 2, the elementary integral model was deduced and established. In Sect. 3, experiments were conducted to calibrate cutting force coefficients and verify the effectiveness of the proposed model. In addition, the propeller baldes machining forces were simulated with two other cutting force models and the simulation efficiency and accuracy were compared.

2 The Elementary Function Integral Model of 5-Axis Machining Forces

2.1 The Deducing Process Based on Mechanical Model

In the light of the assumption that milling force is proportional to the instantaneous undeformed chip thickness, to each differential element of cutting edge, the mechanical milling force model is expressed in the form of Eq. (1).

$$dF_{q,j}(z) = K_q h\, db(z) \tag{1}$$

Where $q = r, t, a$, $K_q(h)$ is radial, tangential and axial cutting force coefficient, $h_j(\psi, z, t)$ is undeformed chip thickness and $db(z)$ is undeformed chip width.

The IUCT model only considering fixed orientation translational feed mode [1]:

$$h(\theta_L, \theta_T) = \frac{F}{nN}\cos\theta_L \sin\kappa \sin\varphi - \frac{F}{nN}\sin\theta_L \cos\kappa \tag{2}$$

where, θ_L is the lead angle of cutter axis. κ, φ are axial and radial contact angle locating the cutting edge element in CCS. N is the number of cutter flute. n is the RPM. F is the cutter feed rate.

The instantaneous undeformed chip width:

$$db(z) = \frac{dz}{sin\kappa} \tag{3}$$

Subsequently, the resulting force components are obtained by summing up the elemental cutting forces for all in-cutting tool elements by performing a numerical integration along the engaged cutting edge in machining process,

$$\left[F_{x,y,z}(\varphi)\right] = \int_{j=1}^{N} \left\{ \int_{z_{1,j}}^{z_{2,j}} \boldsymbol{A}\, dF_{q,j}(z) \right\} \tag{4}$$

where, A is a matrix defined as

$$\boldsymbol{A} = \begin{bmatrix} -\sin\kappa\sin\varphi & -\cos\varphi & -\cos\kappa\sin\varphi \\ -\sin\kappa\cos\varphi & \sin\varphi & -\cos\kappa\cos\varphi \\ \cos\kappa & 0 & -\sin\kappa \end{bmatrix}$$

substituting Eqs. (1), (2) and (3) into Eq. (4), comprehensive considering these constitutive relations and Eq. (4) was simplified into

$$\begin{aligned} \left[F_{x,y,z}(j,\varphi)\right] &= \sum_{j=1}^{N} \int_{z_{1,j}}^{z_{2,j}} \boldsymbol{A}\, dF_{q,j}(z) \\ &= \sum_{j=1}^{N} \int_{z_{1,j}}^{z_{2,j}} \boldsymbol{A}\, K_q \left(\frac{F}{nN} cos\,\theta_L\, sin\kappa\, sin\varphi - \frac{F}{nN} sin\,\theta_L\, cos\kappa \right) \frac{dz}{sin\kappa} \\ &= \sum_{j=1}^{N} \frac{F}{nN} \left\{ cos\theta_L\, P_\varphi - sin\theta_L\, P_\kappa \right\} \end{aligned} \tag{5}$$

where: P_φ and P_κ are middle parameters related to the position of cutter flute and the corresponding forces coefficients, and described as

$$P_\varphi = \int_{z_{1,j}}^{z_{2,j}} \boldsymbol{A}\, K_q\, sin\varphi\, dz$$

$$P_\kappa = \int_{z_{1,j}}^{z_{2,j}} \boldsymbol{A}\, K_q\, cot\kappa\, dz.$$

2.2 The Cutter Flute Model

Figure 1 shows the bull-nose milling cutter model. The observation of a variety of tools shows that the radial contact angle of the cutter edges in the arc segment of the bull and ball nose milling cutter change very little. So it could be assumed that the radial contact angle φ of the cutter edges in the arc segment involved in cutting is constant. Besides, the side edges' axial contact angle κ of the cutter are constants. The calculation of κ and φ of the cutter edges in the arc segment and the side edges are as follows:

The axial contact angle κ of the side edges of the cutter is constant. And in the arc segment, the relationship of axial contact angle κ and axial high z of the cutter edges is described in Eqs. (6) and (7).

$$cos\kappa = \frac{r-z}{r},\ sin\kappa = \frac{\sqrt{r^2-(r-z)^2}}{r} \tag{6}$$

$$z = r - r\ cos\kappa,\ dz = r\ sin\kappa d\kappa \tag{7}$$

Where, the r represents bull-nose fillet radius.

For the cutters with constant pitch, the radial contact angle φ of the cutter edges in the arc segment and the side edges of the cutter is described in Eq. (8).

$$d\varphi = mdz,\ \varphi = \varphi_0 + mz,\ m = -\frac{2\,tan\beta_0}{D} \tag{8}$$

Where, the φ_0 represents the sum of spindle rotation angle and the teeth angle, m describes the pitch.

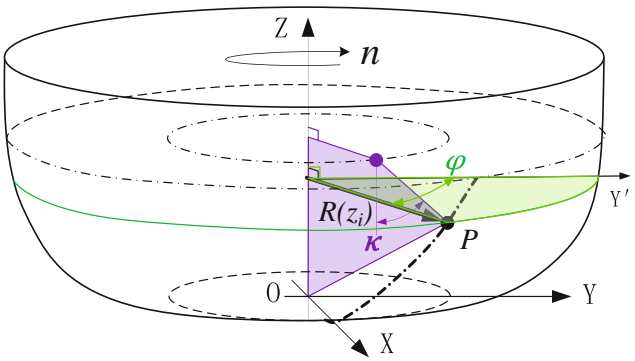

Fig. 1. The bull-nose milling cutter model

2.3 The Calculation of P_φ and P_κ

The calculation of $\boldsymbol{P_\varphi}$ is deduced as expressed in Eq. 9 according to the cutting force model in Sect. 2.1. The integral results are listed in Table 1 for every sub-part of $\boldsymbol{P_\varphi}$.

$$P_\varphi = \int_{z_{1,j}}^{z_{2,j}} \boldsymbol{A}\, K_q \sin\varphi dz = \int_{z_{1,j}}^{z_{2,j}} \begin{bmatrix} -\sin\kappa\sin\varphi & -\cos\varphi & -\cos\kappa\sin\varphi \\ -\sin\kappa\cos\varphi & \sin\varphi & -\cos\kappa\cos\varphi \\ \cos\kappa & 0 & -\sin\kappa \end{bmatrix} \begin{bmatrix} K_r \\ K_t \\ K_a \end{bmatrix} \sin\varphi dz$$
$$= \begin{bmatrix} -\int_L K_r \sin\kappa \sin^2\varphi\, dz - \int_L K_t \cos\varphi \sin\varphi dz - \int_L K_a \cos\kappa \sin^2\varphi\, dz \\ -\int_L K_r \sin\kappa\cos\varphi \sin\varphi dz + \int_L K_t \sin^2\varphi\, dz - \int_L K_a \cos\kappa\cos\varphi \sin\varphi dz \\ \int_L K_r \cos\kappa \sin\varphi dz - \int_L K_a \sin\kappa \sin\varphi dz \end{bmatrix} \quad (9)$$
$$= \begin{bmatrix} p_{\varphi x1} + p_{\varphi x2} + p_{\varphi x3} \\ p_{\varphi y1} + p_{\varphi y2} + p_{\varphi y3} \\ p_{\varphi z1} + p_{\varphi z2} + p_{\varphi z3} \end{bmatrix} \Bigg|_{z_{1,j}}^{z_{2,j}}$$

Where, K_r, K_t and K_a are radial, tangential and axial cutting force coefficient, φ and κ are the radial and axial cutter contact angle of the edge element, dz is the axial discrete element length. The relationship of φ, κ z and dz of the elements on the cutter flute are expressed in Eqs. 6, 7 and 8. The sub-parts $p_{\varphi n1}$, $p_{\varphi n2}$ and $p_{\varphi n3}$ (n = x, y, z) represent the n-direction parts of $\boldsymbol{P_\varphi}$.

Table 1. Part integrals of $\boldsymbol{P_\varphi}$

	The arc zone of cutter flute	The side zone of cutter flute
$p_{\varphi x1}$	$\frac{K_r \sin^2\bar{\varphi}}{r}\left(\frac{(r-z)}{2}\sqrt{r^2-(r-z)^2}+\frac{r^2}{2}arcsin\frac{r-z}{r}\right)$	$-\frac{K_r \sin\kappa}{2m}\left((\varphi_0+mz)-\frac{1}{2}sin(2\varphi_0+2mz)\right)$
$p_{\varphi x2}$	$\frac{K_t}{4m}cos(2\varphi_0+2mz)$	$\frac{K_t}{4m}cos(2\varphi_0+2mz)$
$p_{\varphi x3}$	$-\frac{K_a}{2r}\left(rz-\frac{1}{2}z^2\right)+\frac{K_a}{4mr}(r-z)\sin(2\varphi_0+2mz)-\frac{K_a}{8m^2r}cos(2\varphi_0+2mz)$	$-\frac{K_a \cos\kappa}{2m}\left((\varphi_0+mz)-\frac{1}{2}sin(2\varphi_0+2mz)\right)$
$p_{\varphi y1}$	$\frac{K_r}{2r}sin(2\bar{\varphi})\left(\frac{(r-z)}{2}\sqrt{r^2-(r-z)^2}+\frac{r^2}{2}arcsin\frac{r-z}{r}\right)$	$\frac{K_r}{4m}\sin\kappa\, cos(2\varphi_0+2mz)$
$p_{\varphi y2}$	$\frac{K_t}{2}\left(z-\frac{1}{2m}sin(2\varphi_0+2mz)\right)$	$\frac{K_t}{2}\left(z-\frac{1}{2m}sin(2\varphi_0+2mz)\right)$
$p_{\varphi y3}$	$\frac{K_a}{4mr}(r-z)cos(2\varphi_0+2mz)+\frac{K_a}{8m^2r}sin(2\varphi_0+2mz)$	$\frac{K_a}{4m}\cos\kappa\, cos(2\varphi_0+2mz)$
$p_{\varphi z1}$	$-\frac{K_r}{mr}(r-z)cos(\varphi_0+mz)-\frac{K_r}{m^2r}sin(\varphi_0+mz)$	$-\frac{K_r}{m}\cos\kappa\, cos(\varphi_0+mz)$
$p_{\varphi z2}$	0	0
$p_{\varphi z3}$	$\frac{K_a}{r}sin\bar{\varphi}\left(\frac{(r-z)}{2}\sqrt{r^2-(r-z)^2}+\frac{r^2}{2}arcsin\frac{r-z}{r}\right)$	$\frac{K_a}{m}\sin\kappa\, cos(\varphi_0+mz)$

Note: $\bar{\varphi}$ is the mean value of φ_{z_1} and φ_{z_2}.

The calculation of $\boldsymbol{P_\kappa}$ is deduced as expressed in Eq. 9 according to the cutting force model in Sect. 2.1. The integral results are listed in Table 2 for every sub-part of $\boldsymbol{P_\kappa}$.

$$P_\kappa = \int_{z_{1,j}}^{z_{2,j}} \boldsymbol{A}\, K_q\, cot\kappa\, dz = \int_{z_{1,j}}^{z_{2,j}} \begin{bmatrix} -\sin\kappa\sin\varphi & -\cos\varphi & -\cos\kappa\sin\varphi \\ -\sin\kappa\cos\varphi & \sin\varphi & -\cos\kappa\cos\varphi \\ \cos\kappa & 0 & -\sin\kappa \end{bmatrix} \begin{bmatrix} K_r \\ K_t \\ K_a \end{bmatrix} cot\kappa\, dz$$

$$= \begin{bmatrix} -\int_L K_r\cos\kappa\sin\varphi\, dz - \int_L K_t cot\kappa\cos\varphi\, dz - \int_L K_a\cos\kappa\, cot\kappa\sin\varphi\, dz \\ -\int_L K_r\cos\kappa\cos\varphi\, dz + \int_L K_t cot\kappa\sin\varphi\, dz - \int_L K_a\cos\kappa\, cot\kappa\cos\varphi\, dz \\ \int_L K_r\cos\kappa\, cot\kappa\, dz - \int_L K_a\cos\kappa\, dz \end{bmatrix}$$

$$= \begin{bmatrix} p_{\kappa x1} + p_{\kappa x2} + p_{\kappa x3} \\ p_{\kappa y1} + p_{\kappa y2} + p_{\kappa y3} \\ p_{\kappa z1} + p_{\kappa z2} + p_{\kappa z3} \end{bmatrix} \Bigg|_{z_{1,j}}^{z_{2,j}} \tag{10}$$

Where, K_r, K_t and K_a are radial, tangential and axial cutting force coefficient, φ and κ are the radial and axial cutter contact angle of the edge element, dz is the axial discrete element length. The relationship of φ, κ z and dz of the elements on the cutter flute are expressed in Eqs. 6, 7 and 8. The sub-parts $p_{\kappa n1}$, $p_{\kappa n2}$ and $p_{\kappa n3}$ (n = x, y, z) represent the n-direction parts of $\boldsymbol{P_\kappa}$.

Table 2. Part integrals of $\boldsymbol{P_\kappa}$

	The arc zone of cutter flute	The side zone of cutter flute
$p_{\kappa x1}$	$\frac{K_r}{mr}(r-z)cos(\varphi_0+mz) + \frac{K_r}{m^2 r}sin(\varphi_0+mz)$	$\frac{K_r}{m}\cos\kappa\, cos(\varphi_0+mz)$
$p_{\kappa x2}$	$-K_t\cos\bar{\varphi}\sqrt{r^2-(r-z)^2}$	$-\frac{K_t}{m}\, cot\kappa\, sin(\varphi_0+mz)$
$p_{\kappa x3}$	$-\frac{K_a\sin\bar{\varphi}}{2r}\left((r-z)\sqrt{r^2-(r-z)^2}+r^2 arccos\left(\frac{r-z}{r}\right)\right)$	$\frac{K_a}{m}\cos\kappa\, cot\kappa\, cos(\varphi_0+mz)$
$p_{\kappa y1}$	$-\frac{K_r}{mr}(r-z)sin(\varphi_0+mz) + \frac{K_r}{m^2 r}cos(\varphi_0+mz)$	$-\frac{K_r}{m}\cos\kappa\, sin(\varphi_0+mz)$
$p_{\kappa y2}$	$K_t\sin\bar{\varphi}\sqrt{r^2-(r-z)^2}$	$-\frac{K_t}{m}\, cot\kappa\, cos(\varphi_0+mz)$
$p_{\kappa y3}$	$-\frac{K_a\cos\bar{\varphi}}{2r}\left((r-z)\sqrt{r^2-(r-z)^2}+r^2\, arccos\left(\frac{r-z}{r}\right)\right)$	$-\frac{K_a}{m}\cos\kappa\, cot\kappa\, sin(\varphi_0+mz)$
$p_{\kappa z1}$	$\frac{K_r}{2r}\left((r-z)\sqrt{r^2-(r-z)^2}+r^2\, arccos\left(\frac{r-z}{r}\right)\right)$	$K_r\cos\kappa\, cot\kappa\, z$
$p_{\kappa z2}$	0	0
$p_{\kappa z3}$	$-K_a\left(z-\frac{1}{2r}z^2\right)$	$-K_a\cos\kappa\, z$

Note: $\bar{\varphi}$ is the mean value of φ_{z_1} and φ_{z_2}.

2.4 The Calculation of Upper and Lower Limits of Integration

In order to verify the validity of the method of cutting force calculation, a modeling method of ball-end mill instantaneous engagement region given by B. Ozturk and I. Lazoglu [11] was referred to get three engagement region boundaries. Figure 2 shows the representation of top, front and detail views of boundaries. In the literature,

boundary-1 is obtained from the intersection of the upper face of the workpiece and the semi spherical cutter, boundary-2 is obtained from the intersection of the currently machined surface and the semi spherical cutter, and boundary-3 is the intersection of previously machined surface and the semi spherical cutter. In this paper, three engagement region boundaries were expressed as the functions of radial contact angle φ of cutting edge element based on the expression method of cutting edge element. As with the assumption that Sect. 2.2 of the cutting edge line, the change of radial contact angle of element of the same cutting edge was neglected. However, for the engagement region boundary model in literature [11] was constrained in ball-end part

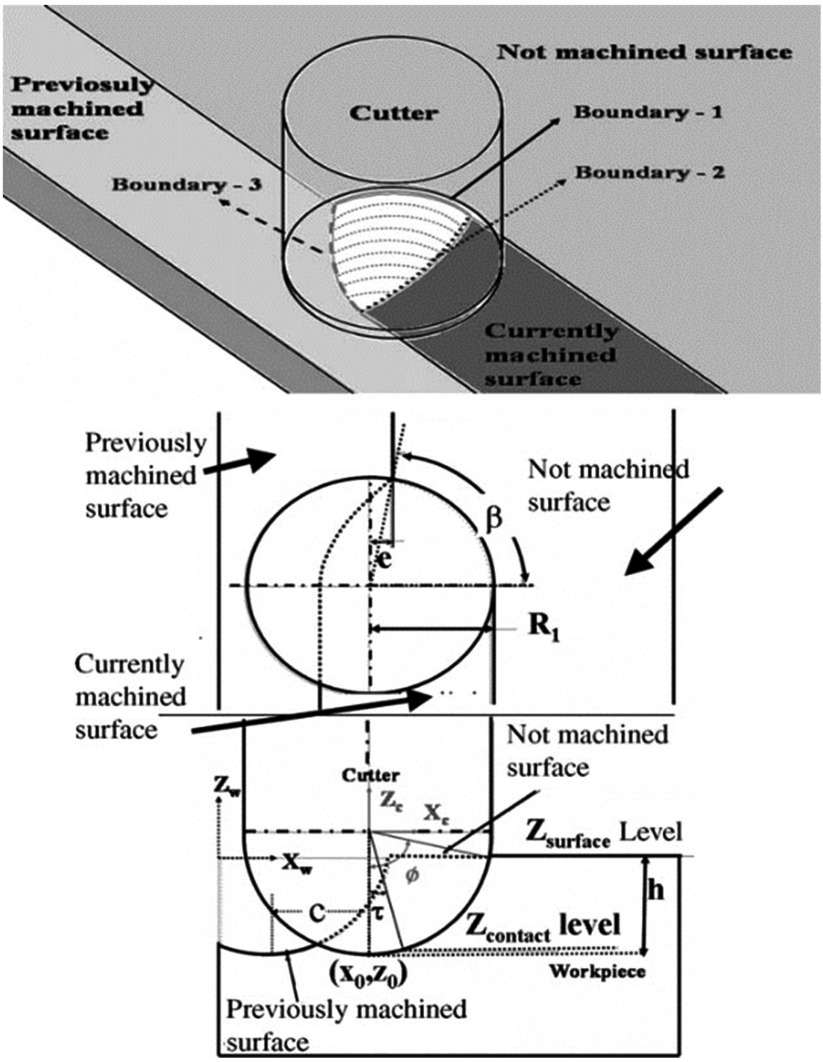

Fig. 2. Top, front and detail views of boundaries [11].

of the cutter and not applied to the side part, the method of calculating the upper and lower limits of integration for ball-end part was given as follows:

For this case, for the specific spindle angle φ_i, the corresponding point of $b_1(\varphi_i)$ of boundary-1, $b_2(\varphi_i)$ of boundary-2 and $b_3(\varphi_i)$ of boundary-3 could be obtained as shown in Fig. 3. When the lead angle $\theta_L \geq 0$, the minimum value between $b_1(\varphi_i)$ and $b_3(\varphi_i)$ was the upper Z values limit of the in-cutting edge in the tool coordinate system and described as z_2, and the $b_2(\varphi_i)$ was the lower Z values limit of the in-cutting edge in the tool coordinate system and described as z_1. When the lead angle $\theta_L < 0$, the maximum value between $b_1(\varphi_i)$ and $b_3(\varphi_i)$ was the lower Z values limit of the in-cutting edge in the tool coordinate system and described as z_1, and the $b_2(\varphi_i)$ was the upper Z values limit of the in-cutting edge in the tool coordinate system and described as z_2.

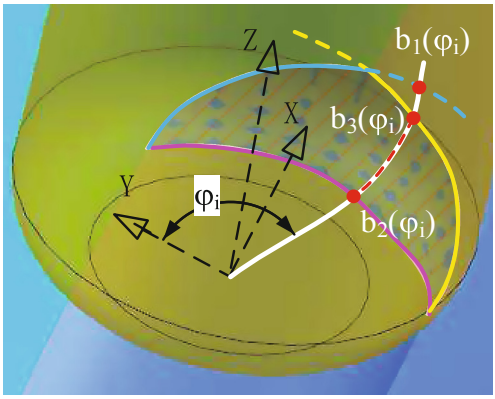

Fig. 3. The upper and lower limits of integration on the flute

3 Experiment Validation and Analysis of the Propeller Blades Machining

3.1 Calibration of Force Coefficients

A single calibration experiment of cutting force coefficient is conducted on *GMC1600H/2 High-speed Precision 5-axis Linkage Gantry Machining Center* with the combination of *Sandvik CoroMill® R216F-12A16C-085* ball nose milling cutter (Table 3) and aluminum alloy 2024-T6. The cutting parameters are set as cutting depth 3 mm, feed rate 500 mm/min, rpm 2000 r/min and down milling with immersion width 5 mm. The force singles are measured and collected using *Kistler 9257A* three-phase piezoelectric crystal dynamometer, *Kistler 5070 type* charge amplifier, and *NI* data acquisition system with sampling frequency 10 kHz. Calibrated milling force coefficients corresponding with varying undeformed chip thickness is shown in Fig. 4, in order to meet the model of this paper, the IUCTs from 0.005 to 0.075 are calculated and the mean coefficients were acquired:

$$\begin{cases} K_t = 2088 \\ K_r = 1653.8 \\ K_a = -161.6 \end{cases} \tag{12}$$

Table 3. cutter parameters

diameter (mm)	Fillet radius (mm)	Flute number	body half taper angle (deg.)	orthogonal rake angle (deg.)
12	6	2	1.33	0

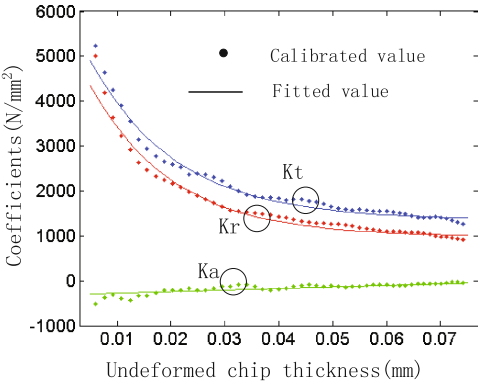

Fig. 4. The cutting force coefficients curve

3.2 Cutting Forces Experiment Validation of Propeller Blades Machining

In order to validate the effectiveness and accuracy of the proposed cutting force model, propeller blades surface was machined with lead angel and tilt angel using ball end mill in this experiment. The model of blades and experiment site are shown in Fig. 5. Cutting parameters were set as follows: cutting width 1.602 mm, feed rate 500 mm/min, spindle speed 2000 r/min. one of the tool paths was pictured in Fig. 5 and recorded in Table 4, which listed the cutter location and orientation.

Three models were utilized to predict the cutting forces: the model established by R. Zhu in literature [5], which using z-map method to determine CWE state, the model establish by B. Ozturk in literature [11], which using CWE boundary method to determine edge element cutting state, and the model in this paper. These models were computed with an identical discrete size but for no discrete required in axial direction of cutters in the method of this paper. The simulation results were drawn in Fig. 6 and the simulation time were recorded in Table 5. As shown in Fig. 6, good prediction accuracy was acquired for all of these three models, especially for the model using z-map method. This is mainly due to the fact that the CWE boundary method in

Ozturk's model and this paper simplify the workpiece surface to a normal plane of local coordinate system. From Table 5 which drawn the simulation time, we could find Ozturk's model is superior to R. Zhu's model in predictive efficiency, and the model in this paper had the best performance, which is faster nearly 20 times and 86 times compared with these two models. Mainly because the model in this paper is based on Ozturk's boundary model and superior to that for the cutting forces are calculated in a cutting flute but not infinitesimal element.

Table 4. The cutter location (CL) file of a tool path

CL No.	X	Y	Z	I	J	K
1	9.4555	35.1119	−13.3606	−0.1683	−0.1135	0.9792
2	12.2993	32.4690	−12.4651	−0.1658	−0.1232	0.9784
3	15.1896	30.0161	−11.5884	−0.1616	−0.1322	0.9780
4	18.1281	27.7572	−10.7281	−0.1559	−0.1403	0.9778
5	21.1201	25.6936	−9.8804	−0.1491	−0.1474	0.9778
6	24.1721	23.8255	−9.0400	−0.1414	−0.1534	0.9780
7	27.2914	22.1526	−8.2020	−0.1330	−0.1585	0.9784
8	30.4834	20.6736	−7.3626	−0.1240	−0.1628	0.9788
9	33.7532	19.3867	−6.5185	−0.1146	−0.1665	0.9794
10	37.1058	18.2908	−5.6661	−0.1052	−0.1696	0.9799
11	40.5464	17.3848	−4.8021	−0.0957	−0.1724	0.9804
12	44.0811	16.6686	−3.9226	−0.0864	−0.1750	0.9810
13	47.7161	16.1421	−3.0235	−0.0775	−0.1776	0.9810
14	49.5723	15.9493	−2.5657	−0.0732	−0.1791	0.9811
15	50.1100	15.9026	−2.4331	−0.0720	−0.1796	0.9811

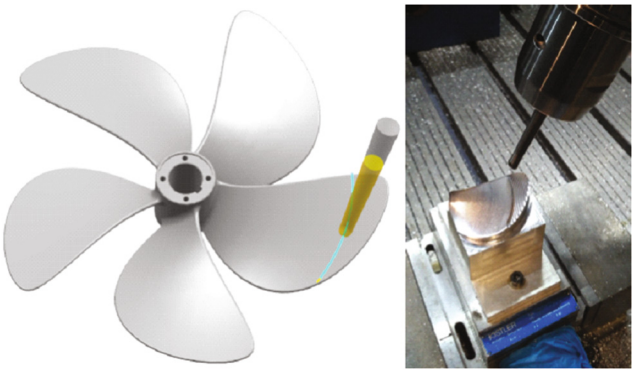

Fig. 5. The model of blades and experiment site

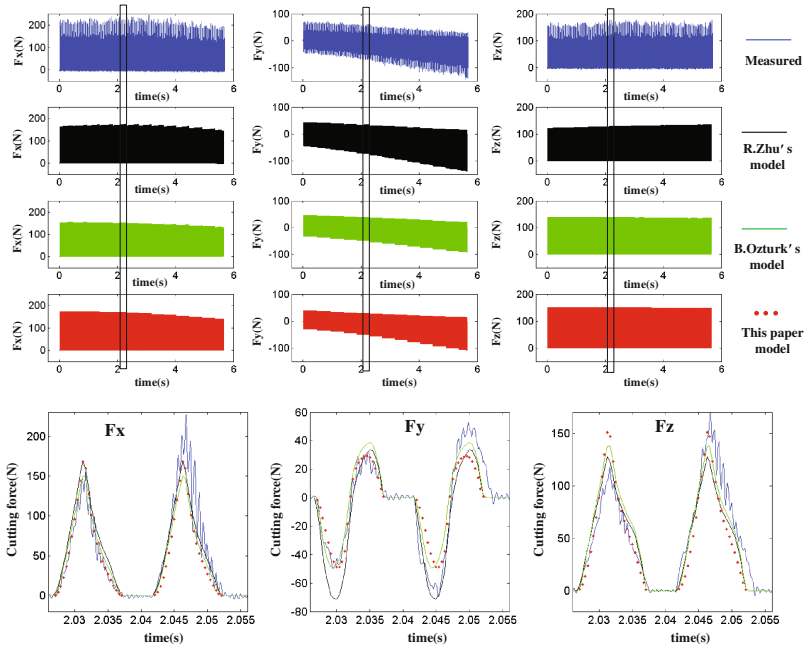

Fig. 6. Comparison between simulated and measured cutting forces

Table 5. Simulation time

Simulation model	Discrete size		Simulation time (s)
	Axial (mm)	Radial (Deg.)	
R. Zhu [5]	0.01	5	534.37
B. Ozturk [11]	0.01	5	123.54
This paper	No discrete	5	6.27

4 Conclusions

This paper proposed an efficient prediction method of multi-axis machining cutting forces, which creatively accomplished the one-off calculation of the cutting force along the whole cutting edge by using integrals of elementary functions in place of classical discretization and accumulation method and avoided both the judgment of cutting state of CEE and repeated calculation of the cutting force for each CEE. Furthermore, the parametric IUCT model considered the cutter orientation angle was used to improve the accuracy in predicting five-axis machining cutting force when transforming classical mechanical force model. Through experiments and simulations on machining of propeller blades, the practicability and efficiency of the method proposed here was verified. Nevertheless, experiments and simulations were confined to the ball-end cutter in this work, please keep on tracking our research for the modeling of the engagement

boundary model for bull-nose mills including the side zone, and the verification of more complex cutting tools like bull nose milling cutters.

Acknowledgements. This research is supported by Major Scientific and Technological Innovation Project of Hubei under Grant no. 2015AAA002, National Natural Science Foundation of China under Grant no. 51421062.

References

1. Zhu, Z., Yan, R., Peng, F., et al.: Parametric chip thickness model based cutting forces estimation considering cutter runout of five-axis general end milling. Int. J. Mach. Tools Manuf **101**, 35–51 (2015)
2. Ferry, W.B., Altintas, Y.: Virtual five-axis flank milling of jet engine impellers—Part I: mechanics of five-axis flank milling. J. Manuf. Sci. Eng. **130**(1), 011005 (2008)
3. Budak, E., Ozturk, E., Tunc, L.T.: Modeling and simulation of 5-axis milling processes. CIRP Ann.-Manufact. Technol. **58**(1), 347–350 (2009)
4. Ozturk, E., Budak, E.: Modeling of 5-axis milling processes. Mach. Sci. Technol. **11**(3), 287–311 (2007)
5. Zhu, R., Kapoor, S.G., DeVor, R.E.: Mechanistic modeling of the ball end milling process for five-axis machining of free-form surfaces. J. Manufact. Sci. Eng. **123**(3), 369–379 (2001)
6. Dongming, G., Fei, R., Yuwen, S.: An approach to modeling cutting forces in five-axis ball-end milling of curved geometries based on tool motion analysis. J. Manufact. Sci. Eng. **132**(4), 041004 (2010)
7. Sun, Y., Guo, Q.: Numerical simulation and prediction of cutting forces in five-axis milling processes with cutter run-out. Int. J. Mach. Tools Manuf **51**(10), 806–815 (2011)
8. Li, Z.-L., Niu, J.-B., Wang, X.-Z., Zhu, L.-M.: Mechanistic modeling of five-axis machining with a general end mill considering cutter runout. Int. J. Mach. Tools Manuf **96**, 67–79 (2015)
9. Larue, A., Altintas, Y.: Simulation of flank milling processes. Int. J. Mach. Tools Manuf **45**(4), 549–559 (2005)
10. Kim, G.M., Kim, B.H., Chu, C.N.: Estimation of cutter deflection and form error in ball-end milling processes. Int. J. Mach. Tools Manuf **43**(9), 917–924 (2003)
11. Ozturk, B., Lazoglu, I.: Machining of free-form surfaces. Part I: analytical chip load. Int. J. Mach. Tools Manuf **46**(7), 728–735 (2006)